Torrent Frog-Inspired Adhesives: Attachment to Flooded Surfaces

*Jagoba Iturri, Longjian Xue, Michael Kappl, Luis García-Fernández, W. Jon P. Barnes, Hans-Jürgen Butt, and Aránzazu del Campo**

Anatomic differences on the toe pad epithelial cells of torrent and tree frogs (elongated versus regular geometry) are believed to account for superior ability of torrent frogs to attach to surfaces in the presence of running water. Here, the friction properties of artificial hexagonal arrays of polydimethylsiloxane (PDMS) pillars (elongated and regular) in the presence of water are compared. Elongated pillar patterns show significantly higher friction in a direction perpendicular to the long axis. A low bending stiffness of the pillars and a high edge density of the pattern in the sliding direction are the key design criteria for the enhanced friction. The elongated patterns also favor orientation-dependent friction. These findings have important implications for the development of new reversible adhesives for wet conditions.

1. Introduction

Natural patterned adhesives have attracted enormous scientific interest over the last ten years.[1] They are conceptually different from classical adhesive formulations. They do not rely on reactive species able to form stable bonds with the contacted surface, but on a particular topographical design at the micro- and nanoscales. The best studied example is the toe pad of the gecko, consisting of several hundred thousand densely packed and highly branched hairs (setae) that allow intimate contact with different substrata and achieve great adhesive strength mainly relying on van der Waals forces.[2]

Less studied, but no less impressive, are frogs' attachment pads. In contrast to geckos, adapted to dry environments, tree frogs are able to attach and climb on vertical and overhanging surfaces without falling.[3] Their toe-pad surface shows a regular hexagonal topography with 10–15 µm epithelial cells separated by ≈1 µm wide channels (**Figure 1**).[3c,4] The surface of each epithelial cell is covered by an array of densely packed nanopillars, ≈300–400 nm diameter, each with a slightly concave top surface.[5] The adhesive mechanism of tree frogs has been extensively investigated,[3a,5c,6] the surface topography being important both for the distribution of fluid across the pad and for the generation of friction forces.[3d] The beneficial role of surface patterns for attachment under wet conditions has also been shown using tree-frog mimics by a few groups.[7] Patterned surfaces showed higher friction forces than flat analogues in the presence of a wetting liquid. The principle behind the enhanced friction was recently elucidated using frog-like polydimethylsiloxane (PDMS) micropatterns.[8] The surface pattern allows draining of the liquid out of the contact area when a shear force is applied, and the establishment of strong direct (dry) contact. Note that both patterned and flat surfaces show poor adhesion in the presence of a wetting liquid, indicating that the surface design of frog toe pads is specialized for hanging or climbing on wet surfaces, where friction forces come into play.

In addition to tree frogs that are largely arboreal, there are also frogs that live around freshwater streams (stream frogs) and waterfalls (rock and torrent frogs) that also possess adhesive toe pads. Biomechanical studies comparing the adhesive abilities of rock and tree frogs of comparable size has shown a significantly superior ability of rock frogs to attach to rough surfaces in the presence of running water.[9] Reported studies on their toe pad morphology revealed anatomic differences from the typical pattern of tree frogs. The toe pad epithelial cells of rock and torrent frogs were elongated[8–10] (Figure 1), with relatively straight channels running across the pad in a distal-proximal direction (white lines on scanning electron microscopy (SEM) images). However, until now there is no experimental evidence that associates elongated patterns with higher adhesion or friction performance in the presence of increasing amounts of wetting liquid. In addition, the elongated pattern suggests that friction properties could be different depending on the friction orientation (along the short or along the long axes of the hexagons). None of these issues have been clarified yet.

In this work, we study the frictional properties of elongated (torrent frog-like) PDMS hexagonal pillar patterns in the presence of water, and we compare them to those of regular (tree frog-like) hexagonal patterns. These studies demonstrate a positive role of elongated surface designs for wet attachment. We

Dr. J. Iturri, Dr. L. Xue, Dr. M. Kappl, Dr. L. García-Fernández, Prof. H.-J. Butt, Dr. A. del Campo
Max-Planck-Institut für Polymerforschung
Ackermannweg, 55128 Mainz, Germany
E-mail: delcampo@mpip-mainz.mpg.de
Dr. W. J. P. Barnes
Centre for Cell Engineering
Joseph Black Building
University of Glasgow
Glasgow, G12 8QQ, Scotland, UK

DOI: 10.1002/adfm.201403751

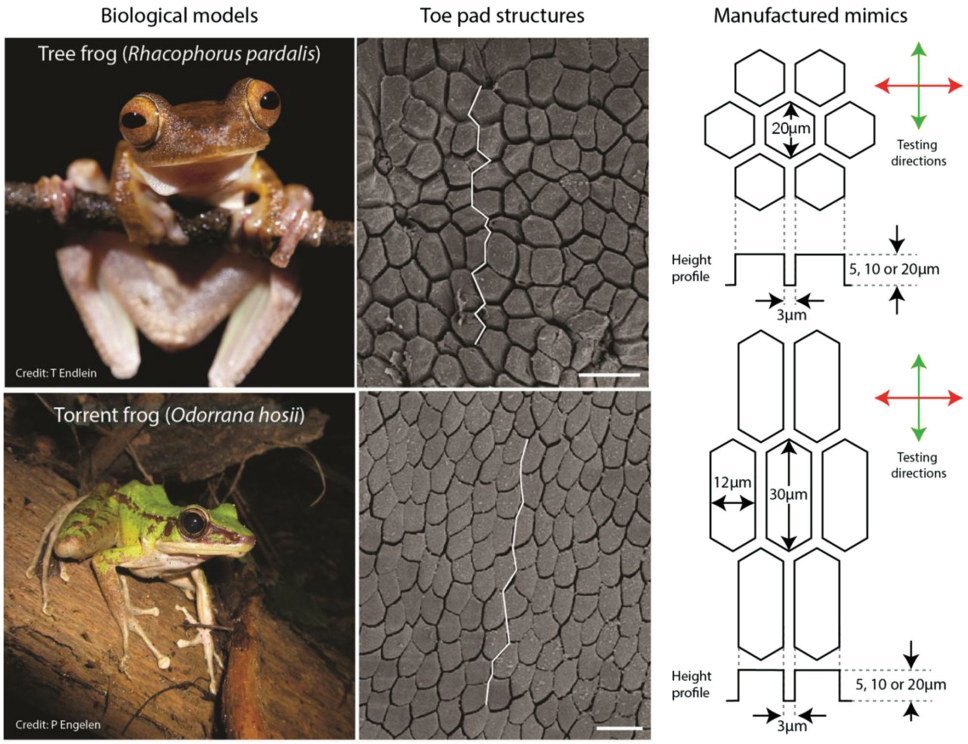

Figure 1. Tree frog *Rhacophorus pardalis* (top left) and torrent frog *Odorrana hosii* (bottom left) and the corresponding SEM images of their toe pad topography showing the regular and elongated hexagonal epithelial cells (middle). Scale bars correspond to 20 µm. The dimensions of the fabricated microstructures are also shown (right), as well as the shear orientations used in the friction experiments. b–d) Representative friction curves measured on different samples under different experimental conditions.

also study the frictional properties of the hexagonal patterns in different shear directions (along a diagonal, or perpendicularly to one edge of the hexagons, Figure 1), in order to elucidate possible orientation-dependent adhesive properties. The obtained results demonstrate superior ability of elongated patterns to attach to wet surfaces, and an orientation-dependent performance. These findings have important implications for the development of new reversible adhesives for wet conditions.

2. Results

2.1. Friction Force Curves

Figure 2b shows a representative friction force curve measured on patterned surfaces using a ruby spherical probe. The raw voltage signal of the lateral (shear) force sensor is plotted against the displacement of the sample in two opposite directions (trace and retrace). The friction curves measured in the two orientations were inversely identical and showed two different regions. Initially, the friction force rapidly increased with increasing lateral displacement but no sliding occurred (static friction). At a certain displacement (gray arrow in Figure 2b), the probe started to slide at a constant friction value (dynamic friction).

When measuring friction curves on flat hydrophobic samples in dry conditions, a saw-tooth like profile was observed (Figure 2c) which was associated with Schallamach according to microscopy observation. Schallamach waves were not observed on hydrophobic microstructured surfaces. Instead, stick–slip events were observed, and disappeared when water was added to the contact surface (Figure 2d,e). Hydrophilic samples (i.e., oxidative plasma-treated hydrophobic samples) showed more pronounced stick–slip behavior than hydrophobic ones (Figure 2d,e). Again, stick–slip vanished in the presence of water (Figure 2e). Thus, water acts as a lubricant that suppresses stick–slip.

On hydrophobic samples the friction force showed a maximum at the static–dynamic transition and dropped in the dynamic range (Figure 2b,d). On hydrophilic samples the transition was smooth and the static and dynamic friction force values were identical (Figure 2e). On hydrophilic samples water is more effectively retained at the interface. It acts as a lubrication layer and facilitates the onset of sliding, thus reducing static friction.

The force sensor voltage values were converted into friction force values using corresponding calibration factors (see Experimental Section and Figure SI1a, Supporting Information, for details). The dynamic friction force values were obtained from the force values at half-distance between the two sliding plateaus ($\Delta V/2$ in Figure 2b). The half-distance acts as "zero" value since the force applied is considered to be the same in trace and retrace directions. The friction force was measured at different normal loads between 1 and 8 mN. Higher loads correspond to higher penetration of the ruby sphere into the elastomer and, therefore, to a larger contact area and a higher friction

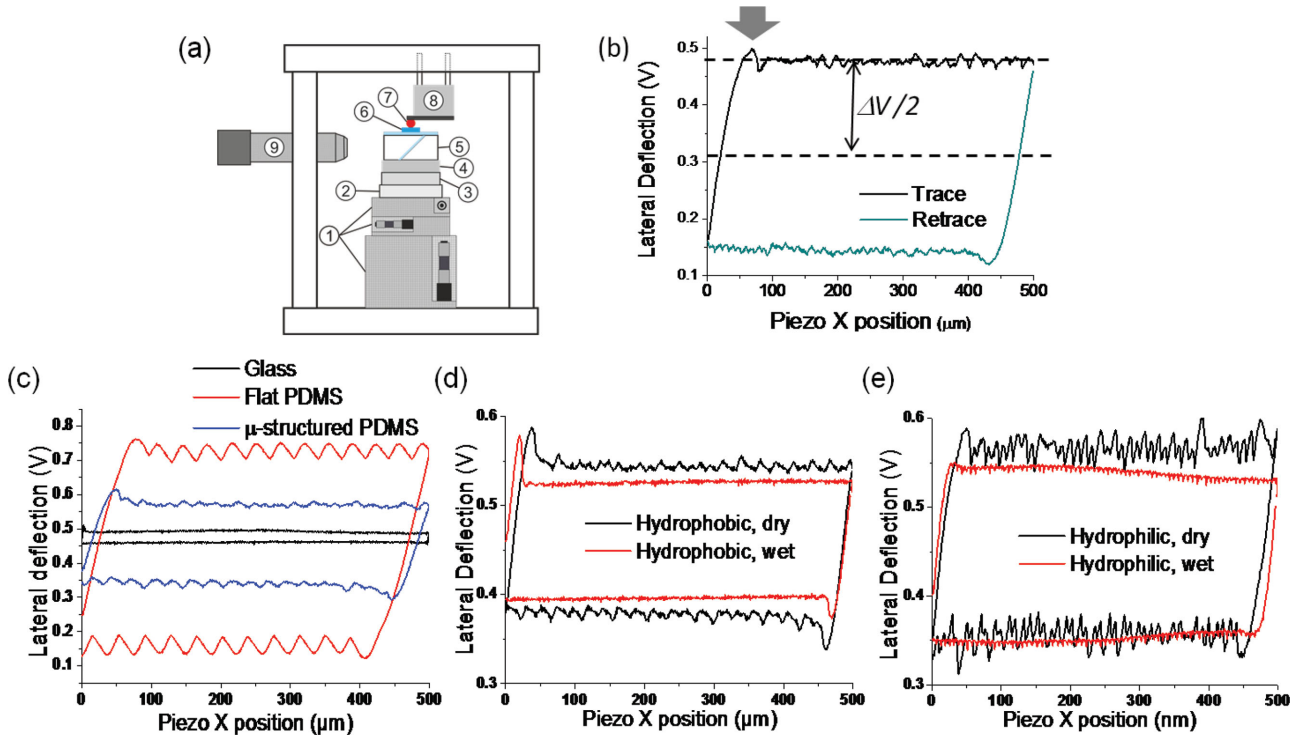

Figure 2. a) Setup for measuring friction forces. A ruby sphere with 4 mm diameter (7) mounted at the end of a vertical thin film load sensor (8) acts as a force probe. The sample (6) sits on top of a sample holder (5) with glass bottom and integrated mirror to allow bottom view via a mirror using the video microscope (9). A motorized xyz-stage (1) allows coarse positioning. During measurements, vertical (2) and lateral (3) piezo translation stages are used to move the sample and friction forces are recorded by the lateral thin film force sensor (4). Motion control and signal acquisition are done by a computer with an AD/DA board running a self-written LabView program. b) Lateral force sensor signal versus piezo position as obtained in friction experiments on a hydrophobic surface patterned with regular hexagons. The half-distance between dynamic friction plateaus ($\Delta V/2$) corresponds to the dynamic sliding friction force. The gray arrow indicates the transition between the static and the dynamic friction. c) Friction curves for glass and for flat and microstructured PDMS under dry conditions. Friction curves for d) hydrophobic and e) hydrophilic microstructured surfaces under dry and wet conditions.

force (Figure SI1b, Supporting Information). Roughly, a load of 1 mN corresponds to an indentation depth of 2.7 μm (calculated from Hertz model[13], and a contact diameter of 290 μm (≈18 pillars in contact) as observed during the friction experiment by optical microscopy. A load of 8 mN corresponds to an indentation of 10.9 μm and a contact radius of 488 μm (≈30 pillars in contact).

2.2. Friction on Regular Versus Elongated Hexagonal Patterns

Friction on arrays of regular and elongated hexagonal pillars (height = 5 μm) was tested in two different orientations: along a diagonal or perpendicularly to one edge of the hexagons (Figure 1a). In the elongated pattern, these orientations correspond to the long and short axes of the hexagon. Regular and elongated patterns have comparable apparent and real contact areas. Measurements were performed in the presence and absence of water at the interface and were compared to measurements on flat samples.

We first analyzed the onset part of the friction force curves. The slope of that part of the friction curve is related to the lateral stiffness of the surface. Flat, unstructured surfaces showed slightly higher slope values than patterned ones (Figure SI2, Supporting Information), indicating a higher stiffness. No appreciable difference was found between the shear strength of regular and elongated patterns in samples with height of 5 μm.

Figure 3 compares dynamic friction forces for regular and elongated hexagonal patterns at a load of 1 mN in water; for measurements in dry conditions see Figure SI3, Supporting Information. When measured along the diagonal, friction forces were similar in regular and elongated patterns. Friction in the direction perpendicular to the edge was higher on both arrays: ≈50% on regular hexagons and more than 100% on elongated ones. The results were similar on hydrophobic and hydrophilic structured samples, in agreement with previously reported results.[8] In contrast, on flat hydrophilic surfaces, friction was much lower. The observed tendencies were also maintained at higher loading forces (Figure SI4, Supporting Information). These results demonstrate the benefit of an elongated hexagonal pattern versus a regular or a non-structured one for friction under wet conditions. The difference in friction forces in the two perpendicular orientations was significantly larger in elongated patterns than on regular ones, indicating that elongated patterns also favor orientation-dependent friction.

Macroscopic testing of the comparative performance of elongated versus regular hexagonal patterns or flat substrates for wet friction was obtained by mounting the PDMS samples

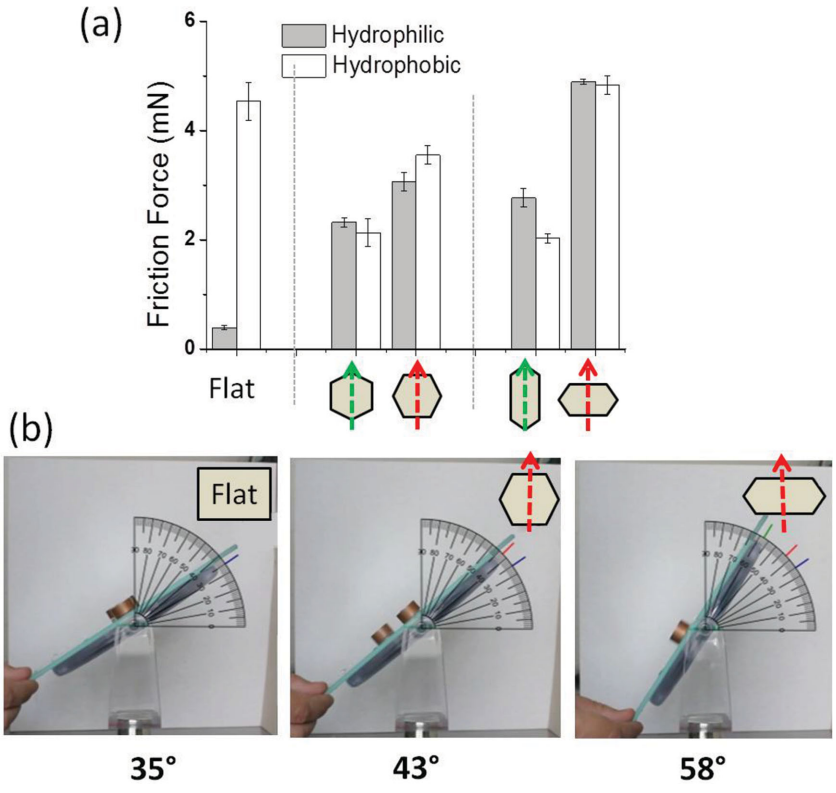

Figure 3. a) Dynamic friction forces for different sample geometries and orientations measured at 1 mN load. Measurements on hydrophilic and hydrophobic PDMS patterns in the presence of water are shown. Friction force values in dry conditions are shown in Figure SI3, Supporting Information. Error bars indicate the standard deviation. b) Snapshot images of Video 1 showing the angles at which flat and micropatterned hydrophilic samples (regular and elongated hexagonal pillars) slide on a tilting stage flooded with water. The PDMS samples are mounted on metal blocks for the experiment.

(flat and structured) on a metal piece and placing them on the surface of a tilting stage that was flooded with water. The stage was tilted gradually and the sliding angle for the different samples was measured. Video 1, Supporting Information, shows the experiment and Figure 3b shows snapshot images during sliding of the different samples in the direction perpendicular to the edge of the hexagons. The sliding angle, i.e., the tilting angle at which the probe started sliding across the flooded surface, was 35°, 43°, and 58° for the flat, regular hexagonal, and elongated hexagonal patterns, respectively. The corresponding calculated downhill forces were 140, 167, and 208 mN for the corresponding normal loads of 201, 179, and 130 mN (the size of the contact areas was 0.49 cm^2). The superior friction performance of an elongated hexagonal patterned surface in wet conditions was thereby demonstrated.

Previous work has demonstrated that in the presence of water the surface microstructure has two effects on the friction performance. (i) The hexagonal channel structure allows drainage of the liquid out of the contact surface during shear.[8] Liquid drainage is a prerequisite for the establishment of dry contact between the tip of the pillars and the probe. (ii) The edges of the microstructures in contact arrest crack propagation, leading to higher peeling forces on structured substrates than on flat controls.[14] In the following paragraphs, we will discuss the influence of the elongated geometry on these two contributions.

The effectiveness of the liquid drainage during shear is expected to depend on two pattern parameters: (1) the channel volume available for liquid flow, and (2) the liquid flow pattern. In our patterns, the channel volume was roughly the same in the regular and elongated hexagonal geometries (10^{-4} cm^3 total channel volume in 1 cm^2 micropillar array with 5 µm height). Therefore, it cannot explain the observed differences in friction force.

During sliding, the micropillars that come into contact with the probe are bent and deformed. The bending stiffness of a microstructure is related to its moment of inertia, *I*. In regular hexagonal pillars, the values of the moment of inertia along the diagonal or perpendicularly to one edge of the hexagon are equivalent (see Figure SI5, Supporting Information, for details on this calculation and Figure SI6, Supporting Information, for the calculated values). The moment of inertia of elongated hexagonal pillars along the long axes is I = 12 281 μm^4 and along the short axes is I = 3320 μm^4. The higher flexibility (smaller bending stiffness) of the elongated hexagonal pillars along their short axes allows them to retain contact with the sliding sphere over longer sliding distances. This leads to higher friction forces, in agreement with the experimental observation. Note that this deformation did not cause permanent sticking or collapse of the pillars in the patterns with 5 µm height. The micropillars recovered to the initial position when the shear forces were removed.

Surface microstructures have been demonstrated to arrest crack propagation during detachment by peeling.[14,15] The effectiveness of the crack arrest is expected to increase with the edge density per unit length along the friction direction. In our patterns, the direction of highest edge density corresponds to the short diagonal of elongated hexagons, which also showed the highest friction forces (Figure 3 and Figure SI3, Supporting Information). The prominent contribution of the edges to the total friction force is also apparent from friction force experiments that were carried out on the elongated hexagons using atomic force microscopy (AFM). Friction forces between a 17 µm diameter glass sphere and the elongated hexagons were measured on a scale of 50 × 50 μm^2. From these experiments, we obtained friction maps (**Figure 4**), which show the distribution of the friction forces within the scan area. Friction is directly proportional to the measured detector signals in volts. It is obvious, that also at this microscopic scale, friction is higher when scanning perpendicular to the long axis of the elongated hexagons and the friction is highest at the edges of the pillars.

In summary, elongated hexagonal micropatterns show higher friction than regular hexagonal patterns under wet conditions. Low bending stiffness of the pillars and high edge

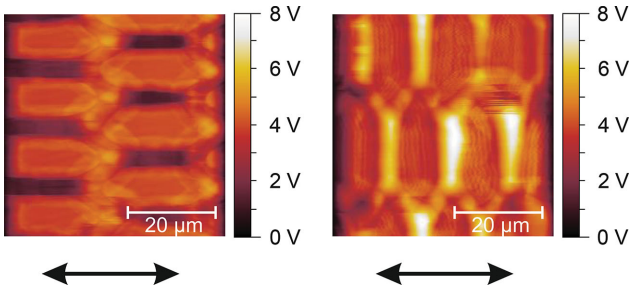

Figure 4. Maps of friction forces between 17 μm diameter glass sphere and the elongated hexagons as measured by AFM. Friction is higher for the scan direction perpendicular to the long axis and always highest along the edges of the pillars.

density of the pattern in the sliding direction seem to be beneficial for high friction surface design. In the elongated patterns, this is maximized when in the orientation perpendicular to the long axes of the hexagons. According to these criteria, arrays of longer and thinner hexagons would lead to higher friction. This possibility is explored in the next section.

2.3. Friction on Elongated Patterns with Increasing Height

The influence of the height of the hexagonal pillars in the friction performance of regular and elongated geometries was studied on patterns with heights 5, 10, and 20 μm; the results presented in the previous sections correspond to patterns with 5 μm height. The slope of the static friction curve revealed the significant decrease in the effective stiffness of the hexagonal patterns with increasing height (Figure SI2, Supporting Information).

In the main, dynamic friction forces obtained on patterns with 10 μm height pillars were not significantly different to those of patterns with 5 μm pillars (**Figure 5**). Only friction forces under non-wetting conditions measured in the direction perpendicular to the edge were smaller when the pillar height increased to 10 μm. This corresponds to the orientation of lowest bending stiffness of the pillars (i.e., highest deformation), and also the orientation of highest pillar–pillar contact area in the deformed state. As a consequence, sticking of neighboring pillars and a decrease in the contact area might occur during the friction experiment. This led to lower friction values, in agreement with measured data. The hydrophobic pattern recovered its initial structure when the shear force was released. For hydrophilic patterns, the higher surface energy led to a higher probability for the pillars to stick to each other.

Friction forces measured on samples with 20 μm height pillars were geometry and orientation independent and approached the values of the friction forces of the flat surface. Microscopic inspection of the samples revealed that the hexagonal pillars stick at their top ends and formed clusters even before shear occurred. Therefore, the frictional behavior of the large pillar blocks approached that of a flat surface. Note that the clustering of pillars was a consequence of the demoulding step during fabrication. This is a well-known effect in PDMS patterns when the aspect ratio increases.[16]

3. Conclusions

Elongated hexagonal patterns show higher friction forces than regular patterned or non-structured surfaces under wet conditions. High pillar deformability and high edge density of the pattern in the sliding direction cause this increase in friction. In the elongated patterns, friction is maximized in the orientation perpendicular to the long axes of the hexagons. However, for very high pillars, high deformation ratios lead to pillar clustering and reduced contact surface. Deformability and mechanical stability need to be balanced in the design of torrent frog-inspired structures with high friction performance, with an optimum of pillar height for a given material stiffness. The elongated patterns also favor orientation-dependent friction. Our findings have important implications for the development of new reversible adhesives for wet conditions.

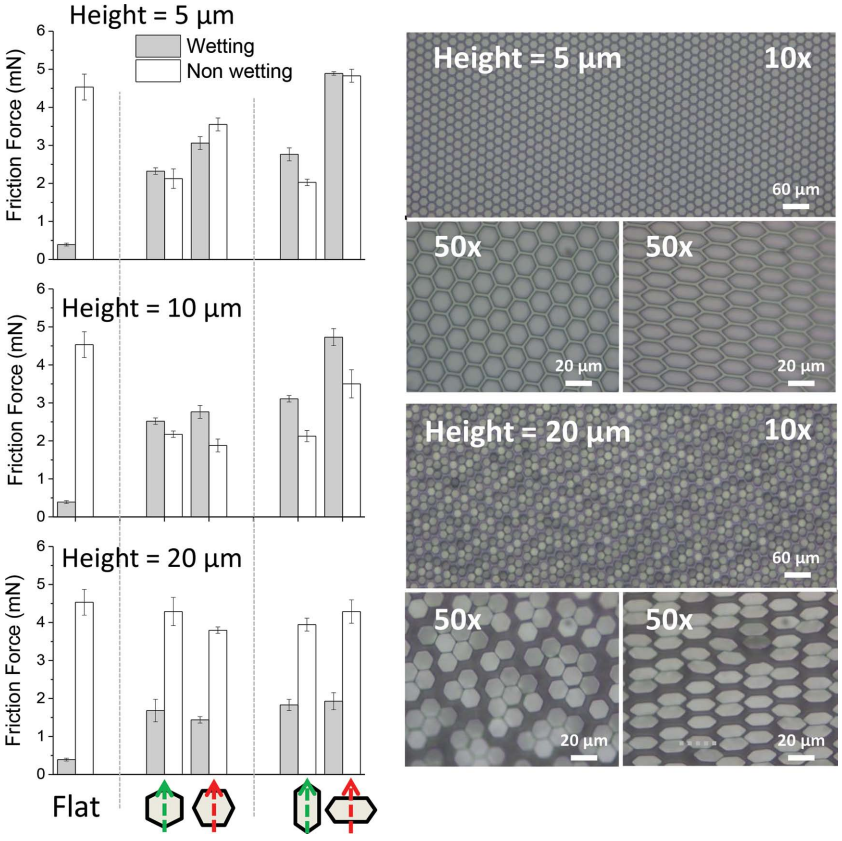

Figure 5. Friction force of flat and patterned samples with increasing heights in the presence of water. Friction forces were measured at 1 mN preload. The optical microscopy pictures show the micropillar arrays with heights of 5 and 20 μm. The pictures at 50× magnification show regular (left) and elongated (right) micropillar arrays.

At this point, it is interesting to compare our results on frog's mimics with previous theories of the functioning of torrent frog toe pads. The toe pad epithelial cells are elongated along the distal/proximal axis of the toes and the resulting straight channels run in the same orientation.[9,10] Since toes are usually placed approximately facing uphill to reduce any tendency for unintentional detachment by peeling,[3c] it has been assumed (though without any supporting experimental evidence) that the orientation of the straight channels would promote good drainage and thus aid the production of high friction forces. This is at odds with the conclusions drawn above where the highest friction is produced by having the long axis of the cells at right angles to the slope. A possible explanation, not tested in the above experiments, is the additional influence of running water, for channels parallel to the water flow are always likely to be more effective than those at right angles to it. Future work will tackle these issues.

4. Experimental Section

Materials and Equipment: Silicon wafers (100 orientation) were provided by Crystec (Berlin, Germany). SU-8 photoresist types 2005 and 2010 covering a thickness range from 5 to 20 µm and the developer mr-Dev 600 were provided by Micro Resist Technology (Berlin, Germany). Hexadecafluoro-1,1,2,2-tetrahydro-octyltrichlorosilane was purchased from ABCR (Karlsruhe, Germany). Masks for lithography were provided by ML&C (Jena, Germany) in quartz with 0.7×0.7 cm^2 chrome patterned fields. PDMS prepolymer Sylgard 184 was purchased from Dow Corning (MI, USA). A mask aligner MJB 3 UV 400 (Süss MicroTec Lithography, Garching, Germany) was used for lithography. A PL-360 LP filter (Omega optical, Brattleboro, USA) was used for cutting wavelengths shorter than 350 nm during the exposure step. A spin-coater WS-650SZ-6NPP/LITE/IND (Laurell Technologies Corporation, North Wales, USA) was used for preparation of photoresist films. Baking steps were carried out on a Präzitherm heating stage (LHG, Düsseldorf, Germany). The profiles of the microstructures were measured with a confocal microscope µSurf C (NanoFocus AG, Oberhausen, Germany). Plasma treatment of samples was carried out with a Plasma Activate Statuo 10 USB chamber (Plasma Technology GmbH, Rottenburg, Germany).

Fabrication of SU-8 Mold Micropatterns by Optical Lithography: Silicon wafers were cleaned in piranha solution (7:3 (v/v) 98%H_2SO_4 /30%H_2O_2) overnight and rinsed with deionized water. Before SU-8 lithographic processing, the wafers were rinsed with acetone and blown dry with nitrogen. The processing parameters are specified in Table SI1, Supporting Information. Patterns fields of 8×8 mm^2 with arrays of hexagonal micropillars (regular and elongated) in hexagonal packing were obtained. Regular micropillars had a diameter of 15 µm (corner-to-corner). The short and long axes of the elongated hexagonal micropillars were 12 and 30 µm (see Figure 1). The height of the pillars was 5, 10, or 20 µm, and the interpillar channels were 3 µm wide. Before being used for soft lithography, the SU-8 patterned wafers were perfluorinated. Samples were treated in oxygen plasma for 10 s (power 100%, gas 100%, pressure 0.1 mbar) followed by silanization in an evacuated desiccator for 30 min using ≈50 µL of 1H,1H,2H,2H-perfluorodecyltrichlorosilane followed by baking for 1 h at 90 °C in a vacuum oven. Silanization increased the contact angle of the cured SU-8 from 73° to 115°. The obtained patterns were used as hard molds for the subsequent soft replication processes with PDMS.

Fabrication of PDMS Pillar Micropatterns by Double Soft-Molding: PDMS precursor (ratio of prepolymer to crosslinker, 10:1) was degassed and poured onto the SU-8 patterned wafer with hexagonal pillars and cured at 90 °C for 1 h in a vacuum oven. The obtained PDMS pattern was the negative replica of SU-8 pattern and was used as a mould for a second replication process. The PDMS replica was perfluorinated using the same condition as described above for the SU-8 pattern. PDMS precursor was cast onto the perfluorinated PDMS soft mold, cured at 90 °C for 1 h and then demoulded. Hydrophilic PDMS samples were obtained by oxidative plasma treatment of the PDMS sample for 10 s (power 100%, gas 100%, pressure 0.1 mbar). Samples were used for the friction experiments immediately after the treatment.

Friction Measurements: Friction forces of flat and microstructured PDMS surfaces were measured using custom-built equipment consisting of a ruby sphere (5 mm diameter) mounted at the end of a cantilever with a thin film force sensor (Figure 2a). The samples were brought into contact with a spherical ruby probe of 5 mm diameter. The lateral (friction) and normal forces between the sample and the sphere were measured. A load of 1 mN (unless different conditions indicated) was applied and kept constant during the measurement using force feedback. Before data collection, pretests were run to set a predefined and constant normal force during the friction. The sample was moved at 100 µm s^{-1} over a distance of 500 µm forward and backward (trace and retrace). The noise of the detection system was less than 10 nN. Measurements were performed in the presence of 0.1 µL of water (unless otherwise indicated) that was applied to the spherical probe using a micropipette. Since the mechanical properties of PDMS may change over time, all friction experiments were performed on freshly prepared samples, fabricated under the same experimental conditions. The laboratory temperature and humidity were recorded for each measurement and were in the range of 20–25 °C and 20%–35% humidity. A minimum of 3–5 measurements on at least three different locations were performed on each sample. Different batches of the same type of microstructure were also analyzed and compared. We characterized the friction behavior of arrays of hexagonal regular (diagonal = 15 µm, height = 5, 10, or 20 µm, interpillar distance = 3 µm) and elongated (diagonal = 30 (long), 12 (short) µm, height = 5, 10, or 20 µm, interpillar distance = 3 µm) micropillars, as well as flat controls. Hydrophobic and hydrophilic samples were tested, in order to investigate the role of surface wettability in friction performance. The measurements were performed in the presence of water and also in dry state. Friction force measurements with an AFM (Dimension 3100, Veeco, Santa Barbara, USA) were carried out on arrays of elongated hexagons. Borosilicate microspheres with a nominal diameter of 20 µm were glued to the end of an AFM cantilever (Budget Sensors, part D, Aluminium reflex coating) using an optical microscope and a micromanipulator to act as a colloidal probe[11] with an epoxy glue (Epikote 1004). The spring constant (k) of the cantilever (k = 40 N m^{-1}) was determined by the thermal noise method.[12] The length of the cantilever was 100 µm, width 50 µm, thickness 2.7 µm. By choosing the scan direction perpendicular to the long axis of the cantilever, the friction between probe and sample leads to a tilt of the cantilever. This tilt is detected by a laser beam that is reflected from the back side of the cantilever onto a photodetector. The detector output signal in volts is directly proportional to the friction force acting on the probe. During scans of the surface of the sample, these lateral tilt signals are recorded for both trace and retrace directions. To obtain friction maps of the scan area, we subtracted the trace from the retrace signals. By changing the sample orientation, we could measure friction forces for scan direction both along and perpendicular to the long axis of the hexagons. The applied load between sphere and sample was kept constant via the feedback loop of the AFM operating in constant force mode. A scan size of 50 µm and a scan rate of 0.5 Hz at different applied loads were used. For each image scan, the trace and retrace signals were recorded. The difference between the trace and retrace signals was calculated using Gwyddion 2.36 software.

Acknowledgements

The authors thank the Deutsche Forschungs Gemeinschaft for financial support within the program SPP1420 "Biomimetic Materials Research: Functionality by Hierarchical Structuring of Materials" (Project Nos. CA880/1, BU 1556/26), Dirk-Michael Drotlef (MPIP) for experimental

help, and Thomas Endlein (U Glasgow) for scientific discussions and graphics support.

Received: October 26, 2014
Revised: December 9, 2014
Published online: January 22, 2015

[1] L. F. Boesel, C. Greiner, E. Arzt, A. del Campo, *Adv. Mater.* **2010**, *22*, 2125.

[2] a) K. Autumn, M. Sitti, Y. C. A. Liang, A. M. Peattie, W. R. Hansen, S. Sponberg, T. W. Kenny, R. Fearing, J. N. Israelachvili, R. J. Full, *Proc. Natl. Acad. Sci. U.S.A.* **2002**, *99*, 12252; b) E. Arzt, S. Gorb, R. Spolenak, *Proc. Natl. Acad. Sci. U.S.A.* **2003**, *100*, 10603; c) A. del Campo, I. Alvarez, S. Filipe, M. Wilhelm, *Adv. Funct. Mater.* **2007**, *17*, 3590; d) A. del Campo, C. Greiner, I. Alvarez, E. Arzt, *Adv. Mater.* **2007**, *19*, 1973; e) A. del Campo, C. Greiner, E. Arzt, *Langmuir* **2007**, *23*, 10235; f) C. Greiner, E. Arzt, A. del Campo, *Adv. Mater.* **2009**, *21*, 479; g) C. Greiner, A. del Campo, E. Arzt, *Langmuir* **2007**, *23*, 3495.

[3] a) W. J. P. Barnes, C. Oines, J. M. Smith, *J. Comp. Physiol. A* **2006**, *192*, 1179; b) S. B. Emerson, D. Diehl, *Biol. J. Linnean Soc.* **1980**, *13*, 199; c) G. Hanna, W. J. P. Barnes, *J. Exp. Biol.* **1991**, *155*, 103; d) W. Federle, W. J. P. Barnes, W. Baumgartner, P. Drechsler, J. M. Smith, *J. R. Soc. Interface* **2006**, *3*, 689.

[4] a) D. M. Green, *Can. J. Zool.* **1979**, *57*, 2033; b) V. Mizuhira, *J. Electron Microsc.* **2004**, *53*, 63; c) S. Chakraborti, D. Das, S. K. De, T. C. Nag, *Acta Zool.* **2014**, *95*, 63.

[5] a) D. M. Drotlef, E. Appel, H. Peisker, K. Dening, A. del Campo, S. N. Gorb, W. J. P. Barnes, *Interface Focus* **2015**, *5*, 20140036; b) W. J. P. Barnes, M. Baum, H. Peisker, S. N. Gorb, *J. Morphology* **2013**, *274*, 1384; c) I. Scholz, W. J. P. Barnes, J. M. Smith, W. Baumgartner, *J. Exp. Biol.* **2009**, *212*, 155.

[6] a) W. J. P. Barnes, P. J. P. Goodwyn, M. Nokhbatolfoghahai, S. N. Gorb, *J. Comp. Physiol. A* **2011**, *197*, 969; b) J. M. Smith, W. J. P. Barnes, J. R. Downie, G. D. Ruxton, *J. Comp. Physiol. A* **2006**, *192*, 1193.

[7] a) M. Varenberg, S. N. Gorb, *Adv. Mater.* **2009**, *21*, 483; b) B. N. J. Persson, *J. Phys.: Condens. Matter* **2007**, *19*, 376110 c) A. Tsipenyuk, M. Varenberg, *J. R. Soc. Interface* **2014**, *11*, 20140113; d) E. Degrandi-Contraires, C. Poulard, F. Restagno, L. Léger, *Faraday Discuss.* **2012**, *156*, 255; e) B. Murarash, Y. Itovich, M. Varenberg, *Soft Matter* **2011**, *7*, 5553; f) J. M. Smith, P. Drechsler, W. Baumgartner, W. J. P. Barnes, W. Federle, *J. R. Soc. Interface* **2006**, *3*, 689; g) R. Gupta, J. Frechette, *Langmuir* **2012**, *28*, 14703.

[8] D. M. Drotlef, L. Stepien, M. Kappl, W. J. P. Barnes, H. J. Butt, A. del Campo, *Adv. Funct. Mater.* **2013**, *23*, 1137.

[9] T. Endlein, W. J. P. Barnes, D. S. Samuel, N. A. Crawford, A. B. Biaw, U. Grafe, *Plos One* **2013**, *8*, e73810.

[10] A. Ohler, *Asiatic Herpetol. Res.* **1995**, *6*, 85.

[11] M. Kappl, H. J. Butt, *Part. Part. Syst. Charact.* **2002**, *19*, 129.

[12] J. L. Hutter, J. Bechhoefer, *Rev. Sci. Instrum.* **1993**, *64*, 1868.

[13] H. Hertz, *J. Reine Angew. Math.* **1882**, *92*, 156.

[14] a) A. Ghatak, *Phys. Rev. E* **2010**, *81*, 021603; b) C. Poulard, F. Restagno, R. Weil, L. Leger, *Soft Matter* **2011**, *7*, 2543.

[15] a) A. Ghatak, L. Mahadevan, J. Y. Chung, M. K. Chaudhury, V. Shenoy, *Proc. R. Soc. London A* **2004**, *460*, 2725; b) J. Y. Chung, M. K. Chaudhury, *J. R. Soc. Interface* **2005**, *2*, 55.

[16] P. Roca-Cusachs, F. Rico, E. Martinez, J. Toset, R. Farre, D. Navajas, *Langmuir* **2005**, *21*, 5542.